Interaction of multiple drops and formation of toroidal-spiral particles

Paola Leon Plata, Ying Liu,* and Ludwig C. Nitsche†
Department of Chemical Engineering, University of Illinois at Chicago, 810 South Clinton Street, Chicago, Illinois 60607, USA

(Received 3 August 2017; published 4 September 2018)

In the development of drug delivery technologies for treating complex diseases, encapsulating multiple compounds and manipulating their sustained-release kinetics independently (for optimal therapeutic effect) can be challenging. Toward this goal, we previously developed a fluid-dynamic technology based on multidrop interactions to produce solid toroidal-spiral (TS) particles. During sedimentation in a miscible, viscous liquid, polymeric drops self-assemble into a reproducible and controllable TS structure, which can be solidified into particles by photoinitiated cross-linking of the polymer. The goal of encapsulating multiple drops of different physical properties (such as size and density) generally requires complicated and time-consuming laboratory iteration on the starting conditions, because all satellite drops (containing drugs) must catch up and coalesce simultaneously with the main drop that forms the surrounding matrix upon solidification. In this paper we consider a model system for multidrop entrainment that features a main drop followed by three smaller satellite drops arranged in a horizontal, triangular array. Experiments visualized with a high-speed camera are used to validate computer simulations based upon a swarm-of-Stokeslets method. The simulations accurately track complex drop configurations involving intertwined interfaces. Replacing the actual starting drop shapes with suitably positioned, volume-equivalent spheres yields very similar configurations: the crucial deformations and interactions occur during sedimentation, as opposed to during the initial injection of the drops. The simulations are then used to formulate two robust "rules of thumb" by which further trial-and-error (whether in the laboratory or by computation) can be avoided toward encapsulating multiple satellite drops with different properties. The first rule applies to satellite drops of different properties but symmetric starting positions, and establishes the single-drop Hadamard-Rybczynski (HR) sedimentation velocity as the crucial parameter. The second rule makes use of a universal "entrainment map" by which three satellite drops of the same radius but different densities and asymmetric starting positions can all be encapsulated at an arbitrarily prescribed distance of sedimentation. Two final simulations demonstrate how both rules can be combined to successfully design an (asymmetric) injection geometry to encapsulate three satellite drops of different radii and densities, at an arbitrarily prescribed distance of sedimentation. Understanding fundamental hydrodynamics of interaction between multiple drops could lead to potential scale-up of production of TS particles and also impact applications of mixing and printing in general.

DOI: 10.1103/PhysRevFluids.3.093601

I. INTRODUCTION

Previous papers [1,2] have combined experiments and computer simulations to study the fluid dynamics of forming polymeric TS structures for (i) single drops, (ii) axisymmetric, vertically displaced

*liuying@uic.edu
†lcn@uic.edu

pairs of drops, and (iii) horizontal, linear multidrop arrays. Potential biomedical applications of this phenomenon have also been established through the laboratory study of drug-release kinetics as well as confirmation of the bioactivity of specific anticancer drug combinations released from TS particles [3]. One example of encapsulating four satellite drops starting in a square array around and above the main drop was also reported [2]. Here our model system for multidrop entrainment involves a horizontal triangular array of satellite drops, with separate pockets encapsulated within the main drop. Our investigation of such heterogeneous structures is motivated by the possibility of (i) encapsulating otherwise incompatible drug mixtures within one drug-delivery particle and (ii) formulating the polymeric compositions to tune the multidrug release kinetics for optimum therapeutic effect. The potential biomedical applications of the two-drug TS particles were demonstrated for the glioblastoma multiforme disease model [2,3]. In this paper we investigate the encapsulation of triangular arrays of satellite drops in quantitative detail. Our aim is to formulate an effective scheme for setting initial conditions for arrays of drops with different properties and to precisely predict the resulting structures after sedimentation and interaction have run their course. In particular, we conduct systematic parametric study to arrive at rules of thumb that reduce experimental trial and error.

The phenomena considered in this paper can be situated in several ways within the voluminous literature on drop dynamics. The shape evolution of the main drop that is advantageous for encapsulating therapeutic drugs to make TS particles represents an early stage in the formation of a miscible vortex ring during sedimentation, which can eventually disintegrate due to a Rayleigh-Taylor instability [4,5]. Experiments on this subject date back to Rogers in 1858 [6], Tomlinson in 1864 [7], Thomson and Newall in 1885 [8], and Northrup in 1912 [9]. These authors explored various combinations and compositions of liquids (affecting density and viscosity), methods of introducing the drop into the bath, and resultant effects upon shape evolution and modes of breakup. For example, Thomson and Newall correlated distance traveled while the ring remained cohesive against the phase of shape oscillation of the drop in free fall just before splashing onto the surface of the bath. They also observed inhibition of ring formation due to interfacial tension attending immiscible drops. Interest in such phenomena gradually reignited with the experiments of Stucke in 1954 [10], Chapman and Critchlow in 1967 [11], and Arecchi *et al.* in 1989 [12] and also the small-deformation and slender-ring asymptotics of Kojima *et al.* in 1984 [13]. Contemporaneously a parallel strand of literature grew around suspension drops [14–26], for which a broad analogy with miscible drops coexists with interesting additional substructural effects arising from particle-scale interactions. For example, Adacchi *et al.* [15], Nitsche and Batchelor [23], Ekiel-Jezewska *et al.* [19], and Alabrudzinski *et al.* [16] provided increasingly refined estimates of the sedimentation velocity of a dilute spherical swarm based upon a point-force representation of the particles. It followed *inter alia* that the settling velocity of an individual particle was vastly exceeded by that of the swarm. Sedimentation of individual particles relative to their local fluid environment, however slow compared to their collective speed, leads to the swarm extending outside the envelope of closed streamlines that would otherwise be analogous to the Hadamard-Rybczynski solution [27,28]. Together with fluctuating particle interactions, this leads to an exodus of particles in a narrow tail [14,23]. In the concentrated regime, the experiments by Arkhipov and Usanina [29] included a novel way of generating the spherical clouds of particles. They measured and correlated drag coefficients for small to $O(1)$ Reynolds number.

A dynamical system representing inertialess interactions between sedimenting point forces (Stokeslets) captures the entire cascade of shapes from initial deformation to formation of a ring to its eventual disintegration and also coalescence and mixing of two trailing blobs [14,21,22]. Of particular interest en route to disintegration is the transition from a closed torus (whose hole is shielded by an envelope of closed streamlines) to an open torus (in which streamlines pass through the hole). Hydrodynamic interaction with a planar wall [30], modeled with the Blake image Stokeslet [31], and polydispersity [32] both reduce time and distance to breakup of the ring.

For vanishing Reynolds number, tracking a sufficiently dense swarm of Stokeslets is formally equivalent to solving the inhomogeneous (i.e., body-force-driven) Stokes equations, an analogy which is numerically useful for modeling liquid drops—especially when the shapes evolve in complicated ways, e.g., involving coalescence and rupture of interfaces [1,2,21,33–36]. With no

corrections to the far-field $O(1/r)$ hydrodynamic interactions, the swarm-of-Stokeslets approach should only be applied to dilute suspension drops: volume fraction $\phi \ll 1$. Inertial effects upon sedimentation of dilute particle swarms were studied by Subramanian and Koch [26] and Pignatel *et al.* [24] via Oseen interactions. The regime of macroscale inertia corresponds to nonnegligible Reynolds number $\mathrm{Re_d}$ based upon the size and settling velocity of the suspension drop while the former is small compared to the inertial screening length. One might attempt to model the swarm as a liquid drop with that Reynolds number, but this is correct only in the limit of particle Reynolds $\mathrm{Re_p} \ll \phi^{1/2}$. Assuming this limit, a further regime of microscale inertia comes in when the inertial screening length diminishes toward the size of the swarm, which means $\mathrm{Re_d} \sim \phi \mathrm{Re_p^{-2}} \gg 1$. When $\mathrm{Re_p} \gg \phi^{1/2}$ there is only the microinertial regime, without intervening Stokes or macroinertial regimes. For dilute swarms, microscale inertia can be modeled with pairwise Oseen (as opposed to Stokeslet) interactions. These show repulsion in all directions except the wake, where there is attraction. In contrast to a Stokeslet swarm (which remains roughly spherical), the collective effect of Oseen interactions is to first dramatically flatten the swarm, and then expand it with a fixed (small) aspect ratio. Subramanian and Koch [26] provided a continuum theory for this behavior and suggested simulations using swarms of Oseen particles. Such simulations were later carried out by Pignatel *et al.* [24]. They found that, by increasing the liquid inertia, the shape instability of the swarm can be accelerated. Although a sufficiently fine swarm of Stokeslets (or suitable regularizations thereof) always provides a good representation of a miscible drop evolving in creeping flow, the parameters involved may or may not apply to a sedimenting swarm of actual particles. Numerics and experiments agree in concluding that inertial effects and particle-scale fluctuations hasten the shape evolution of suspension drops [17,18,20,24]. Finally, for polydisperse suspensions, Faletra *et al.* [37] studied the inhibition of segregation by hydrodynamic interactions and the collective flow. They found good agreement between experiments and computer simulations based upon Oseen interactions.

Immiscible drops pit the restoring influence of interfacial tension against viscous and inertial effects that act unimpeded in miscible drops to produce deformation, ring formation, and eventual breakup. Experiments by Baumann *et al.* [38] showed that higher drop/bath viscosity ratio and Reynolds number were needed to form vortex rings with immiscible drops. Landeau *et al.* [39] characterized the destabilization of immiscible vortex rings at larger Reynolds numbers, extending to the turbulent regime. For viscoelastic drops sedimenting in an immiscible bath, dimpling and formation of toroids have been studied experimentally and via perturbation theory [40] and also numerically by finite differences with front tracking [41]. Miscible (i.e., noncapillary, interdiffusing) interfaces can also manifest (transient) interfacial tension [42]; its influence on drop dynamics and interactions has received attention in the literature [43,44]. Extensive discussion of phenomena and literature surrounding sedimenting vortex rings can be found in the monograph by Joseph and Renardy [4] and a review paper by Meleshko *et al.* [45]. The latter provides a notably historical perspective spanning 150 years and over 200 references. An extraordinarily extensive annotated bibliography (exceeding one thousand entries) on vortex dynamics [46] devotes its Sec. 2.4 to vortex rings.

Several recent papers have considered immiscible liquid tori in flows other than sedimentation. Stationary ring shapes (including streamlines) and time evolution in an axisymmetric compressional flow were modeled with variational and boundary integral methods, respectively, for unit viscosity ratio [47] and then arbitrary viscosity ratio [48,49]. A similar variational approach was applied to stationary liquid rings in a uniform electric field for the same progression of viscosity ratios [50,51]. To directly form liquid tori of arbitrary aspect ratio, Pairam and coworkers [52–54] injected a viscous or nematic liquid over one revolution within a rotating immiscible bath. Depending on the aspect ratio, they observed collapse into a single drop or Rayleigh-Plateau breakup into multiple drops. The tori could be stabilized by comprising the bath of a yield-stress liquid.

By way of summary on sedimentation of miscible and suspension drops, an overarching conclusion is that an initial deviation from spherical shape is required to start the instability that passes through entrainment and ring formation to breakup in creeping flow. Higher Reynolds numbers accelerate the progression and can even cause the cascade starting from a spherical shape. Our manufacture of TS particles arrests the configurational evolution at an early stage and occurs in the former regime.

Aside from sedimenting vortex rings, the present work can also be situated more generally within the literature of drop dynamics. A geophysical motivation for much theoretical and experimental work in this area is the motion and interaction of bubbles in magmas and lavas and also rising mantle plumes [55–59]. For buoyancy-driven versus imposed flows, respectively, the Bond number and capillary number are the crucial dimensionless groups that represent the competition between viscous forces acting to deform the drops and interfacial tension tending to restore a spherical shape (to minimize surface area):

$$\mathrm{Bo} = \frac{(\Delta\rho)ga^2}{\sigma}, \quad \mathrm{Ca} = \frac{\mu V}{\sigma}. \tag{1}$$

One can regard the Bond number as the capillary number into which has been inserted the characteristic buoyant or sedimentation velocity scale in creeping flow. Although transient interfacial tension can exist between miscible, interdiffusing liquids [42], immiscible versus miscible drops are usually distinguished by finite versus infinite Bond number.

For creeping flow, boundary integral and boundary element methods are particularly prominent in the computational modeling of drop deformation and interaction [60–66]. Meshing interfaces instead of the volumes that they enclose reduces the total number of elements and their geometric complexity, although with the burden of tracking and adaptive refinement. For buoyancy-driven motion at various Bond numbers, Davis [60] treated axisymmetric interactions between trailing drops. A series of papers by Manga, Stone, and coworkers progressed with three-dimensional boundary integral numerics from two-drop systems [57,67] to multidrop arrays up to ten [55,68] and also treated hydrodynamic interactions with solid walls and deformable interfaces [58,69]. Griggs *et al.* [70,71] considered the influence on buoyant drop motion of an inclined, planar wall. For drops in Poiseuille flow, they modeled parallel walls and their influence on velocity and lateral migration [72]. Axisymmetric squeezing of a drop through a ring constriction was modeled by Ratcliffe *et al.* [73]. Zinchenko and Davis [74] considered constrictions formed by two discs and two or three spheres. Boundary element methods (BEM) have progressed to model emulsions sedimenting and subjected to shear or extensional flows [56,75–78] and even squeezing through the interstices of granular porous media [79–83].

Interfacial fine structures are also resolvable with front tracking methods in both two-dimensional and axisymmetric cases [41,84–91] and fully three-dimensional geometries [92]. The underlying flow solver typically uses the finite-difference or finite-volume method, and has been implemented for the Navier-Stokes equations and also viscoelastic fluids. Sophisticated, adaptive meshing for boundary elements [60,71,82,93,94] and front tracking [92] can closely approach and even calculate through breakup and coalescence of drops. However, extreme stretching, winding and rupture of interfaces and changes of topology (as observed with sedimenting vortex rings) seems more amenable to a swarm of Stokeslets owing to the "automatic 'renewal' of the interfacial zone with particles from the interior" [21]. Tracking of (axisymmetric) interfaces as coordinate lines is also inherent to boundary-fitted-grid methods [95–98].

Volumetric methods are geared toward reconstructing interfaces on a Eulerian grid instead of Lagrangian tracking. These include level-set methods [99–104], the volume-of-fluid (VOF) method [105–111], the diffuse-interface method, [112,113], and immersed interface methods [114–125]. By avoiding the intricate bookkeeping of connection, disconnection, and reconnection between surface elements, the volumetric, front capturing approach can model very intricate interfacial evolutions. Such methods attain subgrid resolution in one way or another and at various orders of accuracy, but only up to a point. Motivated by the analogy with suspension drops, sedimenting *miscible* drops present a context in which computations based upon a swarm of Stokeslets are uniquely capable. Because of the slow $1/r$ decay of the Stokeslet with distance, the motion of each particle is dominated by far-field interactions, whereas near neighbors contribute only weakly [21,126]. Thus, local fine structures tracked by the particles can result from gross features of the flow field, much as in mixing flows [127]—which would not be the case with capillary interfaces (finite Bond number). The

(drop-following) Eulerian mesh used for particle-mesh lumping can therefore be *much* coarser than the particulate discretization and still resolve the interfacial fine structures accurately [1,2,35].

Boundary integral and boundary element simulations by Manga and Stone [68] and Zinchenko *et al.* [82] are most closely related to the present work because they treated hyrodynamic interactions between multiple miscible drops at unit viscosity ratio (as we do). This paper fills a knowledge gap in parametric study of multidrop interactions, specifically toward the answering the question: Given three satellite drops of arbitrary sizes and densities, how should their starting configuration be chosen so that they will become simultaneously entrained within a sedimenting main drop with a final multicompartment shape that—upon solidification by cross-linking—produces a TS particle that is suitable for drug-delivery applications? We present an easily applied rule of thumb plus a parametric map with which the desired TS particles can be produced in the laboratory without trial and error on the starting configuration. This methodology, which could readily be applied to other numbers of satellite drops, was not available in the previous literature.

Having situated—within the relevant literature of fluid mechanics—our particular approach to generating multicompartment particles, we now flesh out motivations for and applications of such structures along with related and alternative methods of manufacture. Multicompartment structures are desired for potential applications in chemical and biochemical screening, assays for cells, cell encapsulation, cell culture, cell-free production of proteins, and drug delivery [128,129]. In particular, their capabilities as functional carriers could enable coencapsulation of incompatible encapsulants as well as independently tunable controlled release of individual compounds [2,3,130]. Microfluidic techniques are commonly used to generate multicompartment capsules, based on double or higher-order emulsions, and they allow for control in droplet size, composition, and structure within the capsules. Distinct aqueous droplets can be encapsulated into dual-core and multiple-core capsules using double emulsion with specific design of coflow microfluidic devices [131,132]. Precise flow control and composition of the fluid phases determine the stability of the inner cores allowing the capsule to act as microreactors [133] or with controllable encapsulate release [134]. Incorporation of parallel capillaries (or needles) permits the production of independent compartments with individual shells as nospherical [135] and multicompartmental Janus microcapsules [136] by means of coaxial flow. The flexibility of different internal and external fluids enabled the formation of capsules with diverse topology for multiple drugs as well as coencapsulation of cells. The shapes of microparticles (e.g., pearlike, mushroom, bowl) affects release kinetics for drug delivery applications [137].

Most closely related to our previous papers [1–3], the concept of solidifying vortex rings and other structures formed by droplets upon impact with liquid surfaces has been developed in several directions. Our main drop (made of low molecular weight PEGDA) solidified because of photochemically triggered cross linking with a dissolved initiator. Optional solidification of the entrained, trailing drop (which included sodium alginate in addition to the anti-VEGFR-2 antibody) occurred by gelation in contact with calcium chloride in the bulk solution. Gelation of alginate for the main (and only) drop triggered by calcium chloride, calcium diacetate and/or barium diacetate in the gelation bath has also been used [137–139]. An *et al.* [128] generalized the gelation (vortex ring "freezing") mechanism to nanoclays and silica nanocolloids. Toward smaller sizes and scale-up of manufacture, they also used electrospray technology to generate the droplets to be frozen; see also Ref. [129] in connection with similar production of chitosan-metal hydrogel rings as adsorbents. Systematic tuning of the conditions of drop impact allows control of the shapes formed [1,128,139]. Finally, He *et al.* [130] provide an interesting conceptual contrast to our approach for generating multicompartment particles. Whereas our trailing drop catches up to and becomes entrained in the main drop after sedimenting through a significant distance in the bath, their coextruded drops first coalesce into a multicompartment drop *before* being introduced into the gelation bath. The previous literature appears not to have provided systematic parametric study of simultaneous entrainment of multiple (here, three) trailing, satellite drops with different sizes and densities within a leading, main drop during sedimentation. Our work in this paper, resulting in actionable rules of thumb, would enable such multidrop coalescence in the laboratory without further trial and error on the starting conditions for the drops.

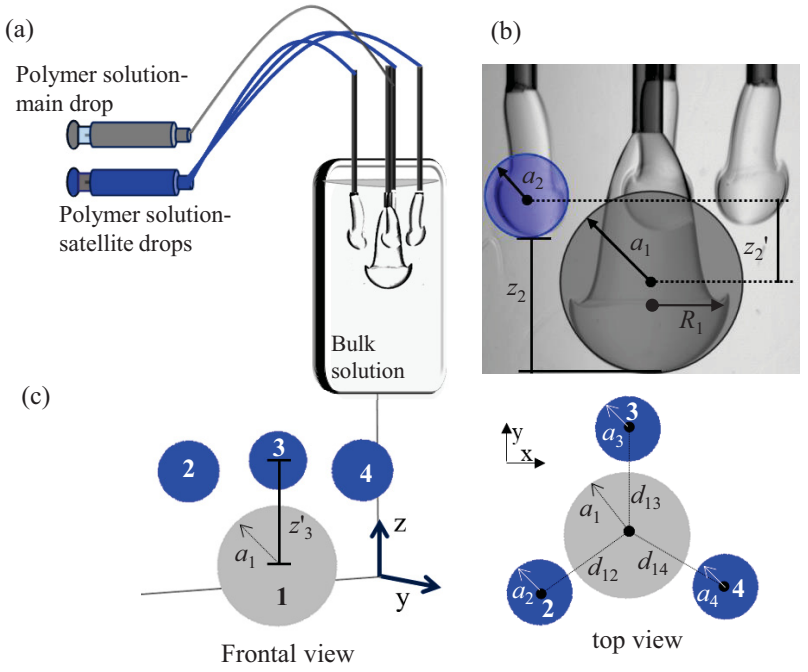

FIG. 1. Starting configuration of four drops. (a) Experimental setup for drop sedimentation and entrainment. Central (main) and surrounding (satellite) drops were infused using syringe pumps with precisely controlled volume. (b) Volume-equivalent spheres were used to represent the droplets in some simulations. Radius a_1 refers to the main drop, whereas a_2, a_3, and a_4 refer to the (smaller) satellite drops. (c) Schematic diagram of the starting configuration of a drop simulation. The bottom-based vertical coordinates z_α are converted to center-based coordinates z'_α for the simulation code. Horizontally projected center-to-center distances $d_{1\alpha}$ between the main and satellite drops match the experiments.

II. MATERIALS AND EXPERIMENTAL SETUP

A. Materials

Poly(ethylene glycol) diacrylate (PEGDA) MW700, glycerol and ethanol were purchased from Sigma-Aldrich (St. Louis, Mo). Water used in all experiments was deionized to 18.2 Ω cm (Nanopure II, Barnstead, Dubuque, IA). All materials were purchased at standard grades and used as received. The viscosities of the (main) polymer drop and surrounding bath solutions have been measured using a rheometer (Physica MCR 302, Anton Paar, Graz, Austria): they are 0.0262 and 0.0312 Pa s, respectively.

B. Experimental setup

The arrangement enables the injection of a main drop surrounded by three smaller satellite drops [Fig. 1(a)]. The polymer concentration of the main drop was higher (83% w/w, PEG-DA 700); that in the satellite droplets was lower, being varied to assess the effects of density and size upon the formation of TS structures. Silicon capillaries (ID: 536.2 μm, OD: 658.3 μm, Polymicro Technologies) were fixed to a triangular geometry, where a central one is surrounded equidistantly by three more. Separately, the central and the neighboring capillaries are connected to syringe pumps that infuse the drops with controlled volume. The central needle was optimized to infuse a volume of 40 μl at 1.2 ml/min and simultaneously each surrounding needle 3.3 μl at 0.3 ml/min. These drops sediment and interact within a bulk solution of glycerol and ethanol that is constituted to

(i) approximately match the drop phase viscosity and (ii) provide a suitable density difference for sedimentation. Further experimental details appear in Sec. I of the Supplemental Material [140].

C. Recording of images

Camera images and videos were captured with a magnification lens (MLH-10X, Computar, Commack, NY) to record drop shapes, multidrop interaction, and confirm droplet encapsulation (Prosilica GX 1050, Allied Vision Technology, Germany). The images were taken at 67 frames per second.

III. NUMERICAL METHOD FOR COMPUTER SIMULATIONS

A. Swarm-of-Stokeslets method

In the experiments the drops sedimented at low Reynolds and their viscosities approximately matched that of the surrounding bath. Under these conditions, the velocity field in and around the drops can be calculated directly by integrating the Green's function of the Stokes equations against the net body force $(\Delta\rho)g$, which is nonzero only within the drops and uniform within each drop α ($\alpha = 1$ for the main drop and $\alpha = 2, 3, 4$ for the satellite drops):

$$\boldsymbol{v}(\boldsymbol{r}, t) = \sum_{\alpha=1}^{4} \int_{\mathcal{V}_\alpha(t)} (\Delta\rho)_\alpha \boldsymbol{g} \cdot \mathbf{G}(\boldsymbol{r} - \boldsymbol{q})\, dV[\boldsymbol{q}]. \tag{2}$$

Here $\mathbf{G}$ is the Stokeslet tensor,

$$\mathbf{G}(\boldsymbol{r}) = (8\pi\mu\|\boldsymbol{r}\|)^{-1}(\mathbf{I} + \|\boldsymbol{r}\|^{-2}\boldsymbol{r}\boldsymbol{r}), \tag{3}$$

with μ the viscosity. The instantaneous shapes of the drops determine the flow field that in turn moves and deforms them, resulting in nonlinear dynamics. Equation (2) has a counterpart in the boundary-integral method [60–68,70,72,74,75,93,94,141–145], wherein the volume integral is transferred to the interfaces [21]. Also in this surface formulation, unit viscosity ratio avoids solution of an integral equation and leaves a simple evolution equation analogous to Eq. (2) [65,68]. The numerical benefit of two-dimensional surface discretization (as opposed to three-dimensional volumetric discretization) diminishes once the interfaces become highly distended and intertwined. This is observed in the experiments, and would require very complicated adaptive remeshing [60,74,93,94,144,145]. Our volumetric, Lagrangian method (essentially a Monte Carlo quadrature scheme) replaces each drop with a statistically uniform swarm of particles, and the volume integral, Eq. (2), is approximated by a sum over point forces. We thus obtain a coupled dynamical system of ODEs for the coordinates of the particles,

$$\frac{d\boldsymbol{r}_i}{dt} = \sum_{j=1}^{M} \boldsymbol{f}_j \cdot \mathbf{G}(\boldsymbol{r}_i - \boldsymbol{r}_j), \tag{4}$$

which is solved numerically with a fourth-order Runge-Kutta scheme. The computations only "know" about the particles: extreme geometric complexity of the evolving interfaces (which represents a visual interpretation on a length scale much larger than the interparticle separation) is incidental and easily handled. Characteristic of particle methods, we can take notably large time steps. The underlying theory and computational methodology—the latter involving a FFT-based particle-mesh scheme to speed up the summations—has been described in previous papers [1,2,21,33–36], to which we relegate details.

B. Dimensionless formulation

To render the simulations dimensionless we use the horizontally projected radius R_1 of the main drop in its starting configuration as the characteristic length and $\mu/[(\Delta\rho)gR_1]$ as the characteristic

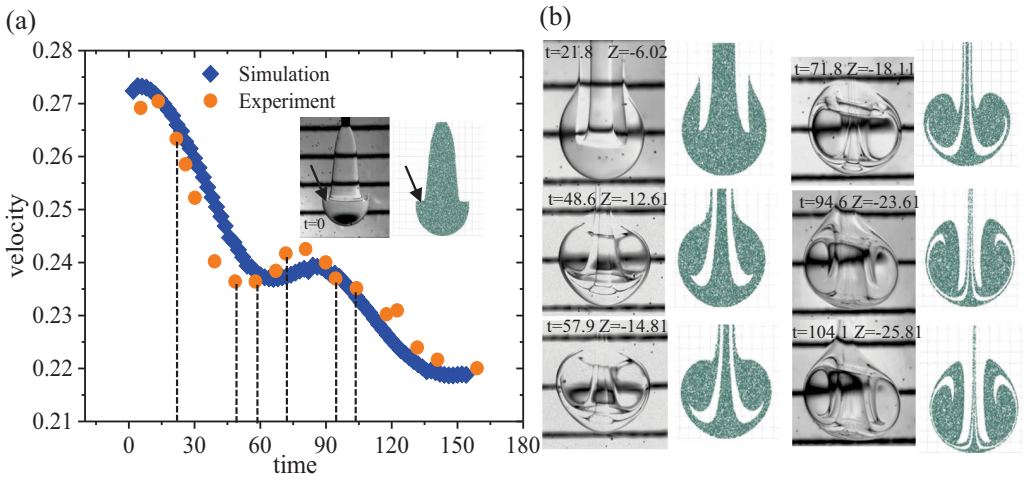

FIG. 2. Single-drop sedimentation, experimental and simulated. (a) Velocity history of the experimental drop compared with a computer simulation of low-Reynolds-number sedimentation flow, starting from a numerical version of the same drop shape (inset, time zero). Velocity and time have been rendered dimensionless as described in the text. (b) Comparison of experimental versus simulated drop shapes at the corresponding (dimensionless) cumulative distances of sedimentation. These correspond to the dimensionless times listed [and identified with dotted lines in part (a)]. In these six images the Reynolds number is within the range 0.0903 to 0.0807.

time. On this dimensionless basis a sphere of unit radius $a = 1$ and uniform body-force density $F = 15/4$ would sediment at unit velocity $v = 1$, according to the Hadamard-Rybczynski (HR) solution [27],

$$v_\alpha = 4Fa_\alpha^2/15, \tag{5}$$

where we have used the subscript α to distinguish the main drop ($\alpha = 1$) from the satellite drops ($\alpha = 2, 3, 4$). The elapsed time to reach a given position is (i) proportional to the viscosity, (ii) inversely proportional to the body-force density, and (iii) inversely proportional to the square of the radius. By matching the vertical position Z of the (bottom of the) main drop between dimensionless simulations and laboratory images, we confirm, within negligible error (see Sec. II in the Supplemental Material [140]), a direct proportionality between dimensionless and laboratory time variables. For validating the simulated evolution of drop configurations, we can therefore use cumulative sedimentation distance as a proxy for time: What is important is to compare the simulated configurations with the laboratory images at the same position Z scaled to the initial drop radius R_1. Similarly, the absolute magnitude of the dimensionless body-force density F is not crucial. What is important is the ratio of body-force density of each satellite drop relative to the main drop: F_2/F_1, F_3/F_1, F_4/F_1. Replacing the sedimentation velocity of the main drop with the HR velocity of a sphere of the same radius at unit viscosity ratio, we arrive at an estimate of the Reynolds number:

$$\mathrm{Re} = 4\rho(\Delta\rho)gR_1^3/[15\mu^2]. \tag{6}$$

Based upon the laboratory parameters the Reynolds number should be small; see Sec. III in the Supplemental Material [140]. On a *post facto* basis, the sedimentation velocities were also determined directly from the laboratory images, using the ruled scale in the background. As listed in the captions of Figs. 2 and 3, the resulting Reynolds number did not exceed 0.1 in the experiments. Thus, we are justified in applying the swarm-of-Stokeslets method to simulate the drop interactions.

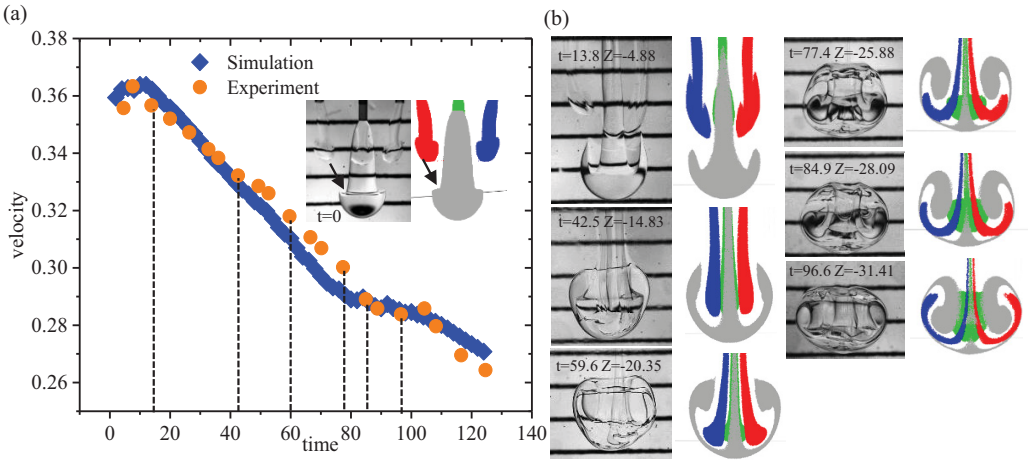

FIG. 3. Four-drop sedimentation, experimental and simulated. (a) Velocity history of four-drop experiment compared with a computer simulation of low-Reynolds number flow, starting from numerical versions of the same drop shapes for the main and satellite drops (inset, time zero). (b) Comparison of experimental versus simulated drop shapes at the corresponding (dimensionless) cumulative distances of sedimentation. These correspond to the dimensionless times listed [and identified with dotted lines in part (a)]. In these six images the Reynolds number is within the range 0.1091 to 0.0858.

C. Simulated drop shapes

Our previous paper [1] detailed the algorithm and assumptions used to convert laboratory images into three-dimensional domains $\mathcal{V}_\alpha$ representing the drops ($\alpha = 1, 2, 3, 4$), from which the volumes V_α could be calculated. Each domain $\mathcal{V}_\alpha$ was then populated with a statistically uniform swarm of N_α Stokeslets, each Stokeslet having force $f_\alpha = F_\alpha V_\alpha / N_\alpha$ in the downward direction, consistent with the dimensionless body-force density F_α. The most realistic simulations of sedimentation would be expected using initial drop shapes converted from the high-speed-camera images taken at the endpoint of injection (Figs. 2 and 3). To form the triangular array of satellite drops, we replicated one of the satellite drops (suitably rotated) at the 120-degree symmetric locations. Some simulations were started with volume-equivalent spheres in place of the satellite drops and even the main drop, which yielded very similar configurational evolutions—especially when compared at the same cumulative distance of sedimentation (Fig. 4). To be precise, we denote with the symbols a_α the dimensionless radii of the volume-equivalent spheres associated with the initial drop shapes ($\alpha = 1, 2, 3, 4$). Note that a_1 is therefore not equal to the horizontally projected dimensionless radius of the main drop—the latter being unity given the lengthscale R_1 defined earlier. The vertically elongated shape implies that $a_1 > 1$ to account for larger volume than would be expected from its horizontal projection. Whenever a volume-equivalent sphere is used in place of the actual drop shape, the vertical coordinate of its center, z'_α, is chosen such that the bottom of the sphere is level with the bottom of the drop, z_α [Fig. 1(b)].

D. Visualization of computer simulations

At any instant the simulated configuration of the drops consists of the Cartesian coordinates of all particles constituting the swarm in 3D space. The direct output of simulations is a sequence of ASCII files containing these coordinates along with numerical codes to flag membership in the main drop or one of the three satellite drops. Each configurational "snapshot" is visualized, whether as a 2D projection or in 3D form, using the R software environment—an open-source package for statistical computing and graphics [146]. To reveal internal features of the evolving TS structure, each image depicts only a subset of the particles lying within a judiciously chosen sectional slice.

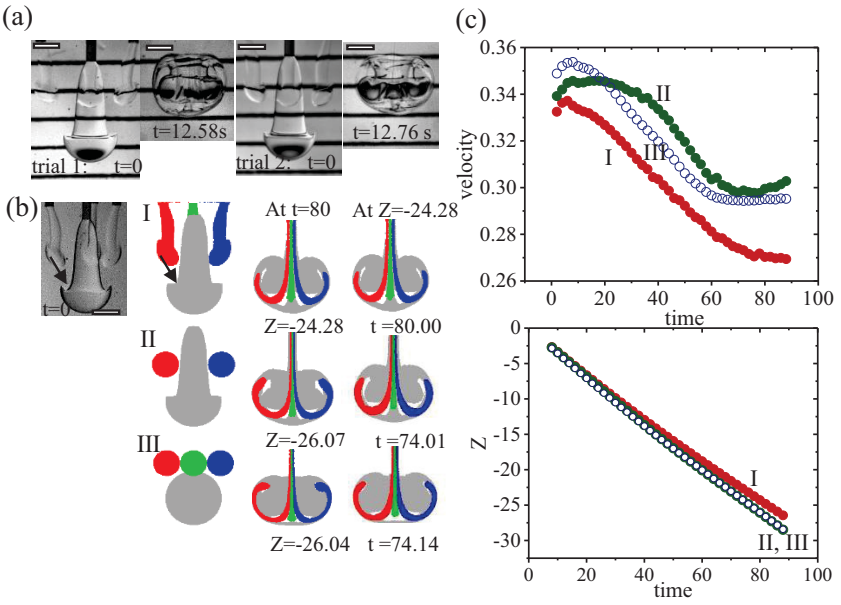

FIG. 4. Four-drop sedimentation in experiments and simulations: reproducibility and sensitivity to initial drop shape. (a) Comparison of high-speed-camera images from two nominally identical experiments. The two images at $t = 0$ indicate reproducibility of the injection process to attain the starting configuration (initial stage), whereas the neighboring images indicate the similarity of the subsequent evolved shape and sedimentation time at the same distance of travel (50 mm). Scale bar represents 2 mm. (b) Simulated effect of initial drop shapes on the configurational evolution. In simulation I, all initial drop shapes were numerically converted from the laboratory image at left. In simulation II, only the main drop is numerically converted from the image, while the satellite drops are replaced with volume-equivalent spheres. In simulation III, all drops are replaced with volume-equivalent spheres. The numerical conversion process was used to estimate the volumes of the laboratory drops as well as their relative positions. The latter determined the horizontal ($d_{1\alpha}$) and vertical (z'_α) drop separations in the simulations. (c) Comparison of velocity and distance histories for the three simulations.

IV. VALIDATION OF THE NUMERICAL SIMULATIONS

In Figs. 2 versus 3 we validate low-Reynolds-number simulations of the evolving configuration of one drop (i.e., the main drop only) versus all four drops, respectively. These calculations account for only sedimentation within an infinite bath of liquid. They do not include, in decreasing order of their expected importance: (i) pressure-driven injection through the needle(s), (ii) possible (minor) mismatches between viscosities of the drops versus surrounding bath, (iii) hydrodynamic effects of the free surface above, or (iv) wall effects due to the surrounding tank. The main drop consists of 40 μl of polymer solution infused within 2 s, and the three smaller satellite drops are also infused within the same time span. Although the drops do significantly deform during the initial infusion, the really complicated and determining configurational evolution occurs afterward, when sedimentation is the only operative phenomenon. There is a tradeoff in selecting a suitable laboratory image to start off each simulation:

(i) The time should be early enough that fluid entrainment in an internal channel (of the type seen in Fig. 2(b) winding around into the characteristic TS shape) has not yet occurred. We are motivated by a restricting assumption in the numerical algorithm for converting 2D laboratory images into the volumetric domains. Conceptually the scheme represents each drop as a "stack" of infinitesimally thin horizontal circular discs "threaded" along a (possibly curved) vertical "backbone." The radius $r(z)$ is therefore assumed to be a single-valued function of z.

(ii) The time should be late enough that infusion has stopped completely. This premise can be checked by estimating the volumes of the image-analyzed drops at various stages.

To put the following elaborations of both aspects into perspective, we preview Fig. 4 to note that sedimentation toward useful TS shapes is remarkably robust to so extreme a perturbation of the initial configuration as replacing the deformed drop shapes with volume-equivalent spheres. Arrows in the inset images in Figs. 2(a), 3(a), and 4(b) show that the simulated starting domain fills in a circumferential depression terminating in a cusp where the laboratory image of the main drop is widest. The associated extra volume can be estimated from half of an elliptic torus (see Sec. IV in the Supplemental Material [140]), and amounts to less than 6% of the total volume of the drop for the frame used to start the simulations. This (i) corresponds to additional mass of liquid that would make the main drop sediment slightly faster, and (ii) represents a minor perturbation of the starting shape that launches the configurational evolution during sedimentation. The former effect actually gets factored out because we compare the laboratory versus simulated images at equivalent distances rather than times.

For the experiment depicted in Figs. 2 or 3, we now consider the selection of "starting" configuration (from among the early-stage laboratory images) with which to launch the corresponding simulation. The start of infusion defines time zero in the laboratory. The starting image was chosen from a laboratory time nominally after the end of infusion, weighing the tradeoff described above. Table I in the Supplemental Material [140] lists several early-stage time points in the experiment, along with the corresponding image-estimated volumes; the choice of starting image is also indicated. Only sedimentation should occur after $t = 2$ s, so the estimated drop volume should level off after this time. What we actually calculated was a relatively small but discernible further increase in volume after the nominal, programed cessation of infusion by the syringe pump. The discrepancy could be due to either continued infusion beyond $t = 2$ s or inaccuracy in the method for estimating 3D volumes from the scanned 2D images. In the former scenario the configurational evolution would be affected by the injection flow, whose contribution is not accounted for in the simulations. In the face of minor misgivings regarding either (i) the fidelity with which the starting drop domains in the simulations represent the actual drops in the experiments, or (ii) possible influence of brief, transient injection effects not modeled in the simulations, the aggregate conclusion of Fig. 2 is very good correspondence between the experiments and simulations—as we shall now describe in detail. Having made the choice of starting configuration, the laboratory "clock" is then reset to zero, and the times listed in the figure refer to dimensionless "simulation time" as converted by the method shown in Fig. I in the Supplemental Material [140]. With time rendered comparable in the experiments versus simulations, we define the sedimentation velocity in terms of cumulative distance traveled by the bottom of the drop, after it has been reduced by its horizontally projected radius in the starting configuration. The experimental versus simulated time histories of the sedimentation velocity show good agreement in Fig. 2(a). At corresponding positions the experimental versus simulated configurations match up well [Fig. 2(b)], although at later stages the simulated TS channel (consisting of entrained liquid) has not wound around quite as far in the simulations. This difference may be due to a mismatch in the viscosities of the drop phase versus surrounding liquid in the experiments; the simulations assume exactly equal viscosities. This aspect is discussed in Sec. V of the Supplemental Material [140].

For a four-drop system optimized for TS formation, Fig. 3 shows similarly good agreement between experiment and simulation. One of the satellite drops has been replicated twice more (and suitably rotated) to generate a triangularly symmetric array in the simulation. Again the velocity histories [Fig. 3(a)] and drop configurations [Fig. 3(b)] match up well. To indicate the degree of reproducibility and variability between laboratory trials, Fig. II in the Supplemental Material [140] repeats Fig. 3 for a nominally identically experiment. In this case the velocity histories happen not to agree as well [Fig. II(a)], although we observe the same general trends in time. However, the simulated configurations do again match the laboratory images quite well at corresponding positions [Fig. II(b)].

V. EFFECT OF INITIAL DROP SHAPES ON CONFIGURATIONAL EVOLUTION AND TS FORMATION

The computer simulations enable parametric analysis that would be tedious or impossible to conduct in the laboratory. Figure 4(b) shows that replacing scanned shapes of the satellite drops and even the main drop with volume-equivalent spheres does not seriously alter the configurational evolutions during sedimentation, provided that we (i) suitably position the spheres and (ii) compare configurations at equivalent positions. Suitable initial positioning means keeping the bottoms of the spheres level with the bottoms of the scanned drop shapes and preserving the horizontally-projected separations based upon the lowest point of each drop. The column of images labeled $Z = -24.28$ shows very similar TS channel shapes for the same cumulative sedimentation distance, although the times to reach this distance vary (within the range $t = 74.01$ to 80) among the three starting configurations. Captured at the same sedimentation time in the column labeled $t = 80$, the sedimentation distances vary (within the range $Z = 24.28$ to 26.07) and the TS channel lengths are slightly different.

Slightly different times to reach the same distance are quantified by the trajectories (Z versus t) in the lower graph in Fig. 4(c). These trajectories for different starting shapes are more similar to each other than the corresponding velocity histories that represent their time derivatives (upper graph). The configurations II and III with satellite or all drops replaced with volume-equivalent spheres sediment faster than the laboratory drops in configuration I (upper graph), but all three curves show roughly similar reductions in velocity as the configurations evolve through entrainment of satellite drops and formation of the TS channels.

We conclude that parametric analysis regarding entrainment of the satellite drops within the main drop and final TS configurations (which applies directly to manufacturing TS particles) can be accurately conducted via computer simulations assuming spherical starting shapes of all drops. In all subsequent simulations the main drop will have radius $a_1 = 1$.

VI. COMPUTER SIMULATION AS A TOOL TO OPTIMIZE TOROIDAL-SPIRAL STRUCTURE FORMATION OF DROPLETS WITH DIFFERENT DENSITIES

Experimental trials established the drop-injection geometry appearing in Figs. 3 and 4, which applies to identical satellite drops positioned in an equilateral triangle around the main drop. Encapsulating multiple, possibly incompatible, drugs into one TS particle will likely entail different densities of the satellite drops and (asymmetric) adjustment of the positions of the injection needles. To avoid tedious trial-and-error in the laboratory, we use computer simulations to validate two robust rules of thumb with which the injection geometry can be easily designed to encapsulate satellite drops of different properties within a suitable TS structure at an arbitrarily chosen distance of sedimentation. The logical argument proceeds in two steps. First, in varying the radius and density of satellite drops, we establish the HR sedimentation velocity as the crucial, correlating quantity. Second, in varying the HR velocity of three identical satellite drops in a symmetrical arrangement, simulations produce an "entrainment map" that indicates how far from the main drop (projected horizontally) the drops should be positioned in order to become entrained in a suitable TS structure at an arbitrarily prescribed distance of sedimentation. With these two heuristics in place, we can immediately design a starting configuration for three satellite drops of arbitrary properties and be assured—without trial-and-error—that they will be successfully encapsulated.

A. Rule #1: HR sedimentation velocity

As a first approximation, we posit that the most important quantity affecting satellite drops' interaction with and entrainment by the main drop is their HR sedimentation velocity—irrespective of how their radius and density conspire to produce that velocity. Obviously, the satellite drops will become deformed during entrainment, but our assumption implies that the main and determining effects are deformation of the main drop and its dominance in determining the overall flow field.

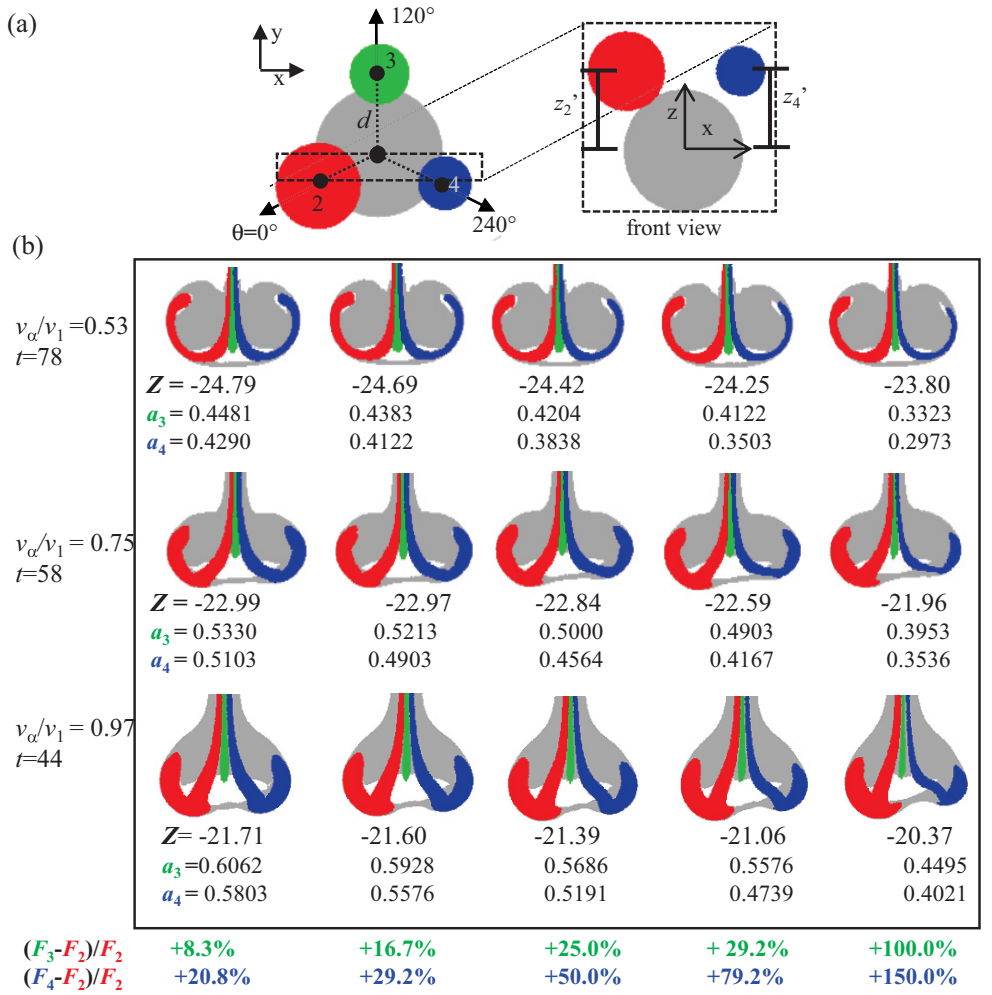

FIG. 5. Tableau of 15 simulations to test the hypothesis that the main determinant of configurational evolution is the HR sedimentation velocity of the satellite drops, irrespective (within reasonable limits) of how their size and force density conspire to produce that velocity. (a) Top view of the four-drop starting configuration (left panel) along with the sectional plane that defines the front view (right panel). The main drop has radius $a_1 = 1$ and force density $F_1 = 1$. Satellite drops are placed at same center-to-center height z'_α and horizontally projected distance ($d_{1\alpha} = d$) from the central drop. The force density F_α of satellite drops increases in the progression from red ($\alpha = 2$) to green ($\alpha = 3$) to blue ($\alpha = 4$). (b) Simulated TS shapes. In all cases the red drop ($\alpha = 2$) has its force density ($F_2 = 2.4$) fixed at the value corresponding to configuration III in Fig. 4(b). In the first row, the radius ($a_2 = 0.47$) also matches the same configuration, which leads to an HR velocity relative to the main drop of $v_2/v_1 = 0.53$. The other two satellite drops have larger force densities and smaller radii. Both parameters are indicated along the bottom of the tableau, color coded to the images. For example, in the upper left image $F_3 = 2.6$ and $F_4 = 2.9$; the respective radii ($a_3 = 0.4481$, $a_4 = 0.4290$) are chosen to yield the same HR velocity: $v_2/v_1 = v_3/v_1 = v_4/v_1$. Progressing down the first column, the HR velocity of the red drop is increased by increasing its radius a_2 at fixed force density ($F_2 = 2.4$). The HR velocity and simulation time for each row is indicated at the left of the tableau. In a given image, all satellite drops have the same HR velocity irrespective of their (differing) sizes, and the distance traveled is indicated. Progressing across each row, we observe that the TS shape is relatively insensitive to the sizes of the satellite drops, provided that they have the same HR velocity. Progressing down each column, we see how the TS shape becomes distorted as the HR velocity increases above the advantageous value observed in the experiments and Fig. 4(b).

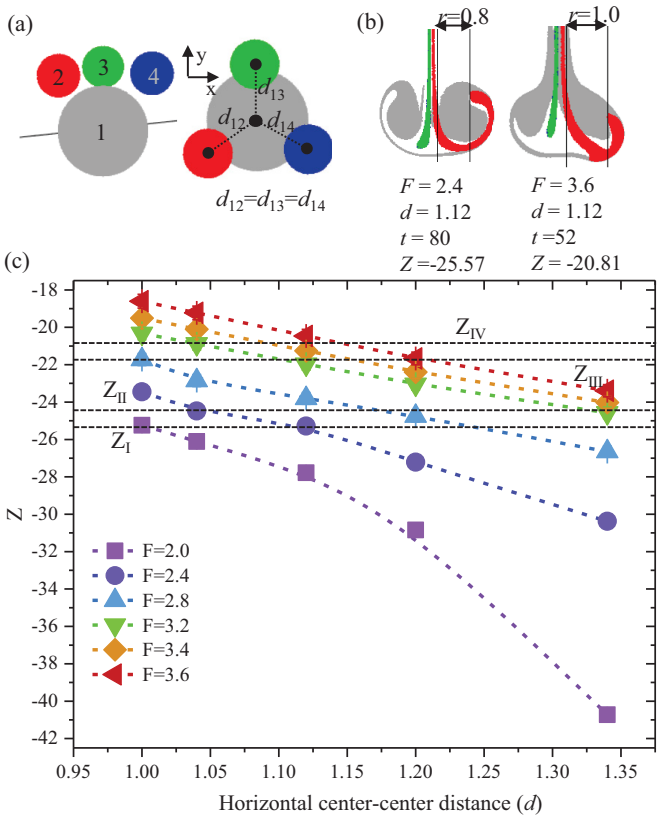

FIG. 6. Entrainment map: curves of travel distance until TS channel formation versus initial horizontal distance of the satellite drops. (a) Initial four-drop configuration with satellite drops of the same radius ($a_2 = a_3 = a_4 = 0.47$) force density ($F = F_2 = F_3 = F_4$) and same center-to center distance ($d = d_{12} = d_{13} = d_{14}$). The main drop has radius $a_1 = 1$ and force density $F_1 = 1$. (b) Visual definition of the "final" stage of TS channel formation used for this comparison. For each value of the force density F, we define the endpoint of shape evolution as that time when the leading tip of the TS channel reaches the top of its curved arc in a sectional view and would subsequently wind further around. To aid in this visual identification, we observe that—irrespective of the initial distance d—this stage occurs when the leading tip comes back to roughly the same radial distance r from the axis, indicated with a pair of vertical lines. Example final configurations (and the endpoint radial distances) are shown for two values of the force density: $F = 2.4, 3.6$. (c) Cumulative distance of travel Z to attain the final TS shape [defined in part (b)] as a function of initial horizontal distance d of the satellite drops for various force densities. The travel distances Z_{I}, Z_{II}, Z_{III}, Z_{IV}, indicated with horizontal lines and enumerated with Roman numerals, refer to the simulations depicted in Fig. 7.

Figure 5(a) shows three satellite drops of different force densities ($F_\alpha/F_1 = \Delta\rho_\alpha/\Delta\rho_1$) and radii ($a_\alpha$) but the same HR sedimentation velocity relative to the main drop: ($v_\alpha/v_1 = F_\alpha a_\alpha^2/F_1 a_1^2$). In order of decreasing radius and commensurately increasing force density, they are color coded red, green, blue. Otherwise, they are positioned in the starting configuration III from Fig. 4(b): center to center height $z_2' = z_3' = z_4' = 1.32$ and horizontally projected distance $d_{12} = d_{13} = d_{14} = 1.12$. Comparing the images along each row of the tableau in Fig. 5(b), we see that the green and blue satellite drops are encapsulated in a roughly symmetric way despite dramatically increasing force density (and decreasing size) compared to the red drop. For comparison, Fig. III in the Supplemental Material [140] shows exactly symmetric configurations. Progressing down the rows, we see that

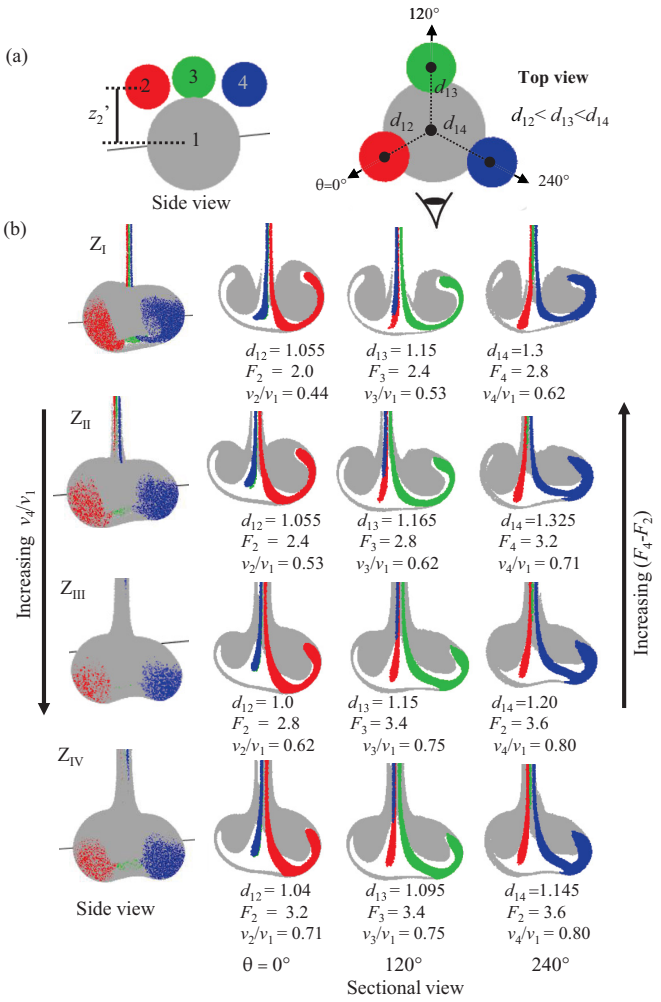

FIG. 7. Tableau of simulated drop configurations illustrates how the entrainment map from Fig. 6 can be used to determine a suitable starting configuration for satellite drops of different HR velocities to come together in a TS shape at an arbitrarily chosen sedimentation distance: Z_I, Z_{II}, Z_{III}, Z_{IV}. (a) Four-drop configuration for satellite drops of the same sizes ($a_2 = a_3 = a_4 = 0.47$) and vertical positions ($z_2' = z_3' = z_4' = 1.32$) but different horizontal distances ($d_{12} \neq d_{13} \neq d_{14}$) and force densities ($F_2 \neq F_3 \neq F_4$). The main drop has radius $a_1 = 1$ and force density $F_1 = 1$. (b) Simulated TS shapes successfully formed at four different sedimentation distances (Z_I, Z_{II}, Z_{III}, Z_{IV}) from satellite drops of different force densities. The leftmost image in each row is a side view from the direction indicated by the eye in part (a). Sectional views from three different angles are indicated in the subsequent three images: each angle emphasizes one of the three satellite drops.

increasing the satellite to main HR velocity ratio above the advantageous value $v_\alpha/v_1 = 0.53$ leads to a distended shape and less effective encapsulation.

B. Rule #2: Entrainment map

Starting from the symmetric initial configuration III in Fig. 4 (center to center height $z_\alpha' = 1.32$, horizontally projected distance $d_{1\alpha} = 1.12$, radius $a_\alpha = 0.47$, force density $F_\alpha = 2.4$), we now consider in Fig. 6 how $d_{1\alpha}$ should be varied to achieve TS encapsulation when we vary the HR

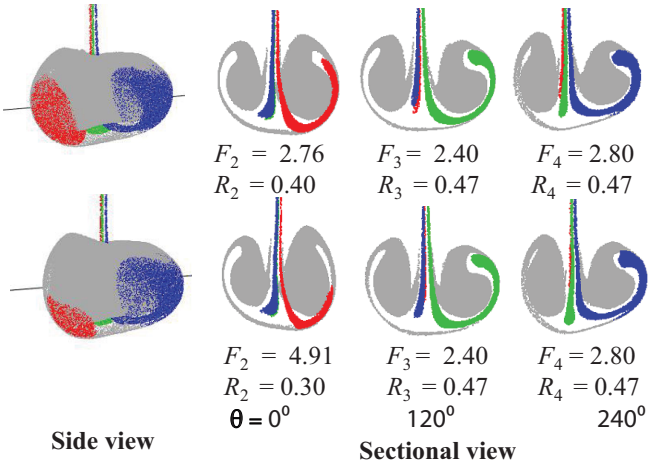

FIG. 8. Demonstration of both rules of thumb used simultaneously to arrive at suitable starting conditions for a case in which the satellite drops have different properties and asymmetric locations. We show simulated TS shapes successfully formed at the same sedimentation distance Z_{I} from Fig. 7(b). All satellite drops are placed at the same horizontal distances as before ($d_{12} = 1.055$, $d_{13} = 1.15$, $d_{14} = 1.3$) and drops 3 and 4 have the same properties. However, the red satellite drop ($\alpha = 2$) now has a smaller radius and commensurately larger body-force density to give the same HR velocity ratio $v_2/v_1 = 0.442$ compared with the red drop in Fig. 7(b). The main drop has radius $a_1 = 1$ and force density $F_1 = 1$.

sedimentation velocity by changing F_α. For fixed F_α (among the values 2.0, 2.4, 2.8, 3.2, 3.4, 3.6), we determine for each starting position $d_{1\alpha}$ the distance Z traveled by an initial four-drop configuration to develop a suitable TS structure, as defined in Fig. 6(b). This leads to the map shown in Fig. 6(c). Using this graph in reverse, we can now decide beforehand at which distance Z (e.g., horizontal dotted lines) we wish the TS shape to form from satellite drops of a given force density F_α and then read off $d_{1\alpha}$ accordingly.

C. TS formation using satellite drops with different HR velocities

Although the entrainment map in Fig. 6(c) was calculated for symmetric starting configurations and satellite drops of the same radius and density, it can be used to formulate a suitable starting condition when the satellite drops have different HR velocities. For drops of equal radii but different densities, Fig. 7 shows how to choose the (asymmetric) horizontal distances of all three drops $d_{1\alpha}$ to be successfully encapsulated within the desirable TS shape at an arbitrarily chosen position Z. For the largest sedimentation distance $Z_{\mathrm{I}} = -26.6$, the TS channels appear quite symmetric even with a 40% spread in force densities between the lightest (red) and heaviest (blue) satellite drops. To achieve encapsulation at shorter distances ($Z_{\mathrm{IV}} = -21.6$), the satellite drops must be heavier with a smaller relative spread in force densities and positioned closer in. A bigger spread in densities can be accommodated if the radius of the densest satellite drop is reduced according to the HR velocity rule. Figure 8 illustrates the design of two (asymmetric) starting configurations when the satellite drops are of different sizes.

VII. CONCLUDING REMARKS

This paper has demonstrated the utility of Stokeslet-based computer simulations in modeling the fluid-dynamic formation of TS structures involving three satellite drops encapsulated within a main drop, which serve as drug-delivery vehicles when photochemically cross-linked into solid particles. Toward formulating a synergistic drug "cocktail" within a single TS particle, parametric

study then established two rules of thumb to avoid experimental or computational trial-and-error in designing the injection geometry when the satellite drops have different sizes and densities. The first rule identifies the HR sedimentation velocity as crucial, independent of how the density and radius conspire to produce that velocity. The second rule involves an entrainment map to determine suitable positions of the satellite drops for encapsulation at an arbitrarily prescribed distance of sedimentation. The combination of experimental and computational methodologies used here could potentially be applied more broadly to mixing and printing phenomena.

ACKNOWLEDGMENT

This work is supported by National Science Foundation DMR program (Grant No. 1404884).

[1] V. Sharma, M. Szymusiak, H. Shen, L. C. Nitsche, and Y. Liu, Formation of polymeric toroidal-spiral particles, Langmuir **28**, 729 (2012).
[2] M. Szymusiak, V. Sharma, L. C. Nitsche, and Y. Liu, Interaction of sedimenting drops in a miscible solution—Formation of heterogeneous toroidal-spiral particles, Soft Matter **8**, 7556 (2012).
[3] V. Sharma, M. Köllmer, M. Szymusiak, L. C. Nitsche, R. A. Gemeinhart, and Y. Liu, Toroidal-spiral particles for codelivery of anti-VEGFR-2 antibody and irinotecan: A potential implant to hinder recurrence of glioblastoma multiforme, Biomacromolecules **15**, 756 (2014).
[4] D. D. Joseph and Y. Y. Renardy, *Fundamentals of Two-fluid Dynamics* (Springer-Verlag, New York, 1993).
[5] M. Shimokawa, R. Mayumi, T. Nakamura, T. Takami, and H. Sakaguchi, Breakup and deformation of a droplet falling in a miscible solution, Phys. Rev. E **93**, 062214 (2016).
[6] W. B. Rogers, On the formation of rotating rings by air and liquids under certain conditions of discharge, Am. J. Sci. Arts **26**, 246 (1858).
[7] C. Tomlinson, On a new variety of the cohesion-figures of liquids, Philos. Mag. **27**, 425 (1864).
[8] J. J. Thomson and H. F. Newall, On the formation of vortex rings by drops falling into liquids, and some allied phenomena, Proc. R. Soc. London **39**, 417 (1885).
[9] E. Northrup, A photographic study of vortex rings in liquids, Nature **88**, 463 (1912).
[10] B. Stucke, Zur Bildung von Wirbelringen, Z. Phys. **137**, 376 (1954).
[11] D. S. Chapman and P. R. Critchlow, Formation of vortex rings from falling drops, J. Fluid Mech. **29**, 177 (1967).
[12] F. T. Arecchi, P. K. Buah-Bassuah, F. Francini, C. Pérez-Garcia, and F. Quercioli, An experimental investigation of the break-up of a liquid drop falling in a miscible fluid, Europhys. Lett. **9**, 333 (1989).
[13] M. Kojima, E. J. Hinch, and A. Acrivos, The formation and expansion of a toroidal drop moving in a viscous fluid, Phys. Fluids **27**, 19 (1984).
[14] G. C. Abade and F. R. Cunha, Computer simulation of particle aggregates during sedimentation, Comput. Methods Appl. Mech. Eng. **196**, 4597 (2007).
[15] K. Adachi, S. Kiriyama, and N. Yoshioka, The behavior of a swarm of particles moving in a viscous fluid, Chem. Eng. Sci. **33**, 115 (1978).
[16] S. Alabrudziński, M. L. Ekiel-Jezewska, D. Chehata-Gómez, and T. A. Kowalewski, Particle clusters settling under gravity in a viscous fluid, Phys. Fluids **21**, 073302 (2009).
[17] T. Bosse, L. Kleiser, J. Favre, and E. Meiburg, Settling and breakup of suspension drops, Phys. Fluids **17**, 091107 (2005).
[18] T. Bosse, L. Kleiser, C. Härtel, and E. Meiburg, Numerical simulation of finite Reynolds number suspension drops settling under gravity, Phys. Fluids **17**, 037101 (2005).
[19] M. L. Ekiel-Jezewska, B. Metzger, and É. Guazzelli, Spherical cloud of point particles falling in a viscous fluid, Phys. Fluids **18**, 038104 (2006).
[20] Y. Lin, J. H. Tan, N. Phan-Thien, and B. C. Khoo, Settling of particle-suspension drops at low to moderate Reynolds numbers, Eur. J. Mech. B/Fluids **61**, 72 (2017).

[21] G. Machu, W. Meile, L. C. Nitsche, and U. Schaflinger, Coalescence, torus formation and breakup of sedimenting drops: Experiments and computer simulations, J. Fluid Mech. **447**, 299 (2001).
[22] B. Metzger, M. Nicolas, and E. Guazzelli, Falling clouds of particles in viscous fluids, J. Fluid Mech. **580**, 283 (2007).
[23] J. M. Nitsche and G. K. Batchelor, Break-up of a falling drop containing dispersed particles, J. Fluid Mech. **340**, 161 (1997).
[24] F. Pignatel, M. Nicolas, and E. Guazzelli, A falling cloud of particles at a small but finite Reynolds number, J. Fluid Mech. **671**, 34 (2011).
[25] U. Schaflinger and G. Machu, Interfacial phenomena in suspensions, Chem. Eng. Technol. **22**, 617 (1999).
[26] G. Subramanian and D. L. Koch, Evolution of clusters of sedimenting low-Reynolds-number particles with Oseen interactions, J. Fluid Mech. **603**, 63 (2008).
[27] J. Happel and H. Brenner, *Low Reynolds Number Hydrodynamics: With Special Applications to Particulate Media* (Kluwer, Amsterdam, 1983).
[28] S. Kim and S. J. Karrila, *Microhydrodynamics: Principles and Selected Applications* (Dover, London, 2005).
[29] V. A. Arkhipov and A. S. Usanina, Gravitational settling of a highly concentrated system of solid spherical particles, Thermophys. Aeromech. **24**, 719, (2017).
[30] A. Myłyk, W. Meile, G. Brenn, and M. L. Ekiel-Jezewska, Break-up of suspension drops settling under gravity in a viscous fluid close to a vertical wall, Phys. Fluids **23**, 063302 (2011).
[31] J. R. Blake, A note on the image system for a Stokeslet in a no-slip boundary, Proc. Cambridge Philos. Soc. **70**, 303 (1971).
[32] T. X. Ho, N. Phan-Thien, and B. C. Khoo, Destabilization of clouds of monodisperse and polydisperse particles falling in a quiescent and viscous fluid, Phys. Fluids **28**, 063305 (2016).
[33] L. C. Nitsche, G. Machu, and W. Meile, Wavelets and fast summations for particle simulations of gravitational flows of miscible drops, Comput. Chem. Eng. **28**, 1873 (2004).
[34] L. C. Nitsche, A. Nguyen, and G. Evans, Globally cohesive drops without interfacial tension, Chem. Phys. Lett. **397**, 417 (2004).
[35] L. C. Nitsche and P. Parthasarathi, Cubically regularized Stokeslets for fast particle simulations of low-Reynolds-number drop flows, Chem. Eng. Commun. **197**, 18 (2010).
[36] L. C. Nitsche and U. Schaflinger, A swarm of Stokeslets with interfacial tension, Phys. Fluids **13**, 1549 (2001).
[37] M. Faletra, J. S. Marshall, M. Yang, and S. Li, Particle segregation in falling polydisperse suspension droplets, J. Fluid Mech. **769**, 79 (2015).
[38] N. Baumann, D. D. Joseph, P. Mohr, and Y. Renardy, Vortex rings of one fluid in another in free fall, Phys. Fluids A **4**, 567 (1992).
[39] M. Landeau, R. Deguen, and P. Olson, Experiments on the fragmentation of a buoyant liquid volume in another liquid, J. Fluid Mech. **749**, 478 (2014).
[40] M. C. Sostarecz and A. Belmonte, Motion and shape of a viscoelastic drop falling through a viscous fluid, J. Fluid Mech. **497**, 235 (2003).
[41] S. Mukherjee and K. Sarkar, Viscoelastic drop falling through a viscous medium, Phys. Fluids **23**, 013101 (2011).
[42] P. G. Smith, T. G. M. van de Ven, and S. G. Mason, The transient interfacial tension between two miscible fluids, J. Colloid Interface Sci. **80**, 302 (1981).
[43] C. Tufano, G. W. M. Peters, H. E. H. Meijer, and P. D. Anderson, Effects of partial miscibility on drop-wall and drop-drop interactions, J. Rheol. **54**, 159 (2010).
[44] T. W. Walker, A. N. Logia, and G. G. Fuller, Multiphase flow of miscible liquids: Jets and drops, Exp. Fluids **56**, 106 (2015).
[45] V. V. Meleshko, A. A. Gourjii, and T. S. Krasnopolskaya, Vortex rings: History and state of the art, J. Math. Sci. **187**, 772 (2012).
[46] V. V. Meleshko and H. Aref, A bibliography of vortex dynamics 1858–1956, Adv. Appl. Mech. **41**, 197 (2007).

[47] M. Zabarankin, O. M. Lavrenteva, and A. Nir, Liquid toroidal drop in compressional Stokes flow, J. Fluid Mech. **785**, 372 (2015).
[48] B. K. Ee, O. M. Lavrenteva, I. Smagin, and A. Nir, Evolution and stationarity of liquid toroidal drop in compressional Stokes flow, J. Fluid Mech. **835**, 1 (2018).
[49] M. Zabarankin, Liquid toroidal drop in compressional flow with arbitrary drop-to-ambient fluid viscosity ratio, Proc. R. Soc. A **472**, 20150737 (2016).
[50] M. Zabarankin, Liquid toroidal drop under uniform electric field, Proc. R. Soc. A **473**, 20160633 (2017).
[51] M. Zabarankin, Toroidal drop under electric field: Arbitrary drop-to-ambient fluid viscosity ratio, Proc. R. Soc. A **473**, 20170379 (2017).
[52] E. Pairam and A. Fernández-Nieves, Generation and Stability of Toroidal Droplets in a Viscous Liquid, Phys. Rev. Lett. **102**, 234501 (2009).
[53] E. Pairam, H. Le, and A. Fernández-Nieves, Stability of toroidal droplets inside yield stress materials, Phys. Rev. E **90**, 021002 (2014).
[54] E. Pairam, J. Vallamkondu, V. Koning, B. C. van Zuiden, P. W. Ellis, M. A. Bates, V. Vitelli, and A. Fernandez-Nieves, Stable nematic droplets with handles, Proc. Natl. Acad. Sci. USA **110**, 9295 (2013).
[55] M. Manga, Interactions between mantle diapirs, Geophys. Res. Lett. **24**, 1871 (1997).
[56] M. Manga, J. Castro, K. V. Cashman, and M. Loewenberg, Rheology of bubble-bearing magmas, J. Volcanol. Geotherm. Res. **87**, 15 (1998).
[57] M. Manga and H. A. Stone, Interactions between bubbles in magmas and lavas: Effects of bubble deformation, J. Volcanol. Geotherm. Res. **63**, 267 (1994).
[58] M. Manga, H. A. Stone, and R. J. O'Connell, The interaction of plume heads with compositional discontinuities in the Earth's mantle, J. Geophys. Res. **98**, 19979 (1993).
[59] R. J. Whittaker and J. R. Lister, The self-similar rise of a buoyant thermal in very viscous flow, J. Fluid Mech. **606**, 295 (2008).
[60] R. H. Davis, Buoyancy-driven viscous interaction of a rising drop with a smaller trailing drop, Phys. Fluids **11**, 1016 (1999).
[61] C. Pozrikidis, The instability of a moving viscous drop, J. Fluid Mech. **210**, 1 (1990).
[62] C. Pozrikidis, *Boundary Integral and Singularity Methods for Linearized Viscous Flow* (Cambridge University Press, Cambridge, 1992).
[63] C. Pozrikidis, Interfacial dynamics for stokes flow, J. Comput. Phys. **169**, 250 (2001).
[64] C. Pozrikidis, *A Practical Guide to Boundary-element Methods with the Software Library BEMLIB* (Chapman & Hall, London, 2002).
[65] J. M. Rallison, A numerical study of the deformation and burst of a viscous drop in general shear flow, J. Fluid Mech. **109**, 465 (1981).
[66] J. M. Rallison and A. Acrivos, A numerical study of the deformation and burst of a viscous drop in an extensional flow, J. Fluid Mech. **89**, 191 (1978).
[67] M. Manga and H. A. Stone, Buoyancy-driven interactions between two deformable viscous drops, J. Fluid Mech. **256**, 647 (1993).
[68] M. Manga and H. A. Stone, Collective hydrodynamics of deformable drops and bubbles in dilute low Reynolds number suspensions, J. Fluid Mech. **300**, 231 (1995).
[69] C. Huber, J. M. Watkins, and M. Manga, Steady shape of a miscible bubble rising below an inclined wall at low Reynolds numbers, Eur. J. Mech. B/Fluids **28**, 405 (2009).
[70] A. J. Griggs, A. Z. Zinchenko, and R. H. Davis, Gravity-driven motion of a deformable drop or bubble near an inclined plane at low Reynolds number, Int. J. Multiphase Flow **34**, 408 (2008).
[71] A. J. Griggs, A. Z. Zinchenko, and R. H. Davis, Creeping motion and pending breakup of drops and bubbles near an inclined wall, Phys. Fluids **21**, 093303 (2009).
[72] A. J. Griggs, A. Z. Zinchenko, and R. H. Davis, Low-Reynolds-number motion of a deformable drop between two parallel plane walls, Int. J. Multiphase Flow **33**, 182 (2007).
[73] T. Ratcliffe, A. Z. Zinchenko, and R. H. Davis, Buoyancy-induced squeezing of a deformable drop through an axisymmetric ring constriction, Phys. Fluids **22**, 082101 (2010).
[74] A. Z. Zinchenko and R. H. Davis, A boundary-integral study of a drop squeezing through interparticle constrictions, J. Fluid Mech. **564**, 227 (2006).

[75] M. Loewenberg and E. J. Hinch, Numerical simulation of a concentrated emulsion in shear flow, J. Fluid Mech. **321**, 395 (1996).
[76] A. Z. Zinchenko and R. H. Davis, Large-scale simulations of concentrated emulsion flows, Philos. Trans. R. Soc. London A **361**, 813 (2003).
[77] A. Z. Zinchenko and R. H. Davis, Extensional and shear flows, and general rheology of concentrated emulsions of deformable drops, J. Fluid Mech. **779**, 197 (2015).
[78] A. Z. Zinchenko and R. H. Davis, An efficient algorithm for hydrodynamical interaction of many deformable drops, J. Comput. Phys. **157**, 539 (2000).
[79] R. H. Davis and A. Z. Zinchenko, Motion of deformable drops through granular media and other confined geometries, J. Colloid Interface Sci. **334**, 113 (2009).
[80] A. Z. Zinchenko and R. H. Davis, Algorithm for direct numerical simulation of emulsion flow through a granular material, J. Comput. Phys. **227**, 7841 (2008).
[81] A. Z. Zinchenko and R. H. Davis, Squeezing of a periodic emulsion through a cubic lattice of spheres, Phys. Fluids **20**, 040803 (2008).
[82] A. Z. Zinchenko and R. H. Davis, Emulsion flow through a packed bed with multiple drop breakup, J. Fluid Mech. **725**, 611 (2013).
[83] A. Z. Zinchenko and R. H. Davis, Motion of deformable drops through porous media, Annu. Rev. Fluid Mech. **49**, 71 (2017).
[84] H. Dogan, S. Nas, and M. Muradoglu, Mixing of miscible liquids in gas-segmented serpentine channels, Int. J. Multiphase Flow **35**, 1149 (2009).
[85] D. Izbassarov and M. Muradoglu, A front-tracking method for computational modeling of viscoelastic two-phase flow systems, J. Non-Newtonian Fluid Mech. **223**, 122 (2015).
[86] M. Muradoglu and S. Gokaltun, Implicit multigrid computations of buoyant drops through sinusoidal constrictions, J. Appl. Mech. **71**, 857 (2004).
[87] M. Muradoglu and A. D. Kayaalp, An auxiliary grid method for computations of multiphase flows in complex geometries, J. Comput. Phys. **214**, 858 (2006).
[88] M. Muradoglu and S. Tasoglu, A front-tracking method for computational modeling of impact and spreading of viscous droplets on solid walls, Comput. Fluids **39**, 615 (2010).
[89] M. Muradoglu and G. Tryggvason, A front-tracking method for computation of interfacial flows with soluble surfactants, J. Comput. Phys. **227**, 2238 (2008).
[90] U. Olgac, A. D. Kayaalp, and M. Muradoglu, Buoyancy-driven motion and breakup of viscous drops in constricted capillaries, Int. J. Multiphase Flow **32**, 1055 (2006).
[91] K. Sarkar and W. R. Schowalter, Deformation of a two-dimensional drop at non-zero Reynolds number in time-periodic extensional flows: Numerical simulation, J. Fluid Mech. **436**, 177 (2001).
[92] S. O. Unverdi and G. Tryggvason, A front-tracking method for viscous, incompressible, multi-fluid flows, J. Comput. Phys. **100**, 25 (1992).
[93] V. Cristini, J. Blawzdziewicz, and M. Loewenberg, Near-contact motion of surfactant-covered spherical drops, J. Fluid Mech. **366**, 259 (1998).
[94] V. Cristini, J. Blawzdziewicz, and M. Loewenberg, An adaptive mesh algorithm for evolving surfaces: Simulations of drop breakup and coalescence, J. Comput. Phys. **168**, 445 (2001).
[95] G. Ryskin and L. G. Leal, Orthogonal mapping, J. Comput. Phys. **50**, 71 (1983).
[96] G. Ryskin and L. G. Leal, Numerical solution of free-boundary problems in fluid mechanics. Part 1. The finite-difference technique, J. Fluid Mech. **148**, 1 (1984).
[97] G. Ryskin and L. G. Leal, Numerical solution of free-boundary problems in fluid mechanics. Part 2. Buoyancy-driven motion of a gas bubble through a quiescent liquid, J. Fluid Mech. **148**, 19 (1984).
[98] G. Ryskin and L. G. Leal, Numerical solution of free-boundary problems in fluid mechanics. Part 3. Bubble deformation in an axisymmetric straining flow, J. Fluid Mech. **148**, 37 (1984).
[99] E. Bassano, Level-set based numerical simulation of a migrating and dissolving liquid drop in a cylindrical cavity, Int. J. Numer. Methods Fluids **44**, 409 (2004).
[100] Y. C. Chang, T. Y. Hou, B. Merriman, and S. Osher, A level set formulation of Eulerian interface capturing methods for incompressible fluid flows, J. Comput. Phys. **124**, 449 (1996).

[101] K. B. Deshpande and W. B. Zimmerman, Simulation of interfacial mass transfer by droplet dynamics using the level set method, Chem. Eng. Sci. **61**, 6486 (2006).
[102] S. J. Osher and R. P. Fedkiw, *Level Set Methods and Dynamic Implicit Surfaces* (Springer, Berlin, 2003).
[103] S. Tanguy and A. Berlemont, Application of a level set method for simulation of droplet collisions, Int. J. Multiphase Flow **31**, 1015 (2005).
[104] J. J. Xu, Z. Li, J. Lowengrub, and H. Zhao, A level-set method for interfacial flows with surfactant, J. Comput. Phys. **212**, 590 (2006).
[105] A. V. Coward, Y. Y. Renardy, M. Renardy, and J. R. Richards, Temporal evolution of periodic disturbances in two-layer couette flow, J. Comput. Phys. **132**, 346 (1997).
[106] D. Gueyffier, J. Li, A. Nadim, R. Scardovelli, and S. Zaleski, Volume-of-fluid interface tracking and smoothed surface stress methods applied to multiphase flow and pendant drop pinching, J. Comput. Phys. **152**, 423 (1999).
[107] S. Hardt, An extended volume-of-fluid method for micro flows with short-range interactions between fluid interfaces, Phys. Fluids **17**, 100601 (2005).
[108] C. W. Hirt and B. D. Nichols, Volume of fluid method for the dynamics of free boundaries, J. Comput. Phys. **39**, 201 (1981).
[109] J. Li, Y. Y. Renardy, and M. Renardy, Numerical simulation of breakup of a viscous drop in simple shear flow through a volume-of-fluid method, Phys. Fluids **12**, 269 (2000).
[110] Y. Renardy and M. Renardy, Prost: A parabolic reconstruction of surface tension for the volume-of-fluid method, J. Comput. Phys. **183**, 400 (2002).
[111] R. Scardovelli and S. Zaleski, Direct numerical simulation of free-surface and interfacial flow, Annu. Rev. Fluid Mech. **31**, 567 (1999).
[112] D. M. Anderson, G. B. McFadden, and A. A. Wheeler, Diffuse-interface methods in fluid mechanics, Annu. Rev. Fluid Mech. **30**, 139 (1998).
[113] P. Yue, J. J. Feng, C. Liu, and J. Shen, A diffuse-interface method for simulating two-phase flows of complex fluids, J. Fluid Mech. **515**, 293 (2004).
[114] W. F. Hu, M. C. Lai, and Y. N. Young, A hybrid immersed boundary and immersed interface method for electrohydrodynamic simulations, J. Comput. Phys. **282**, 47 (2015).
[115] A. T. Layton, An efficient numerical method for the two-fluid Stokes equations with a moving immersed boundary, Comput. Methods Appl. Mech. Eng. **197**, 2147 (2008).
[116] R. J. LeVeque and Z. Li, The immersed interface method for elliptic equations with discontinuous coefficients and singular sources, SIAM J. Numer. Anal. **31**, 1019 (1994).
[117] R. J. LeVeque and Z. Li, Immersed interface methods for stokes flow with elastic boundaries or surface tension, SIAM J. Sci. Comput. **18**, 709 (1997).
[118] Z. Li, An overview of the immersed interface method and its applications, Taiwanese J. Math. **7**, 1 (2003).
[119] Z. Li and M. C. Lai, The immersed interface method for the navier-stokes equations with singular forces, J. Comput. Phys. **171**, 822 (2001).
[120] H. Liu, S. Krishnan, S. Marella, and H. S. Udaykumar, Sharp interface Cartesian grid method II: A technique for simulating droplet interactions with surfaces of arbitrary shape, J. Comput. Phys. **210**, 32 (2005).
[121] Z. Tan, D. V. Le, Z. Li, K. M. Lim, and B. C. Khoo, An immersed interface method for solving incompressible viscous flows with piecewise constant viscosity across a moving elastic membrane, J. Comput. Phys. **227**, 9955 (2008).
[122] Z. Tan, D. V. Le, K. M. Lim, and B. C. Khoo, An immersed interface method for the incompressible Navier-Stokes equations with discontinuous viscosity across the interface, SIAM J. Sci. Comput. **31**, 1798 (2009).
[123] S. Xu and Z. J. Wang, An immersed interface method for simulating the interaction of a fluid with moving boundaries, J. Comput. Phys. **216**, 454 (2006).
[124] S. Xu and Z. J. Wang, Systematic derivation of jump conditions for the immersed interface method in three-dimensional flow simulation, SIAM J. Sci. Comput. **27**, 1948 (2006).
[125] Q. Zhang and P. L.-F. Liu, Handling solid-fluid interfaces for viscous flows: Explicit jump approximation vs. ghost cell approaches, J. Comput. Phys. **229**, 4225 (2010).

[126] M. P. Brenner, Screening mechanisms in sedimentation, Phys. Fluids **11**, 754 (1999).
[127] J. Ottino, Mixing, chaotic advection, and turbulence, Annu. Rev. Fluid Mech. **22**, 207 (1990).
[128] D. An, A. Warning, K. G. Yancey, C. T. Chang, V. R. Kern, A. K. Datta, P. H. Teen, D. Luo, and M. Ma, Mass production of shaped particles through vortex ring freezing, Nat. Commun. **7**, 12401 (2016).
[129] H. Zhou, L. Xu, Y. Wen, K. Lin, and X. Zeng, Ring-like structured chitosan-metal hydrogel: Mass production, formation mechanism and applications, J. Colloid Interface Sci. **490**, 233 (2017).
[130] F. He, W. Wang, X. H. He, X. L. Yang, M. Li, R. Xie, X. J. Ju, Z. Liu, and L. Y. Chu, Controllable multicompartmental capsules with distinct cores and shells for synergistic release, ACS Appl. Mater. Interfaces **8**, 8743 (2016).
[131] A. Perro, C. Nicolet, J. Angly, S. Lecommandoux, J. F. Le Meins, and A. Colin, Mastering a double emulsion in a simple co-flow microfluidic to generate complex polymersomes, Langmuir **27**, 9034 (2011).
[132] H. C. Shum, Y. J. Zhao, S. H. Kim, and D. A. Weitz, Multicompartment polymersomes from double emulsions, Angew. Chem., Int. Ed. **50**, 1648 (2011).
[133] H. Chen, Y. Zhao, J. Li, M. Guo, J. Wan, D. A. Weitz, and H. A. Stone, Reactions in double emulsions by flow-controlled coalescence of encapsulated drops, Lab Chip **11**, 2312 (2011).
[134] W. Wang, T. Luo, X. J. Ju, R. Xie, L. Liu, and L. Y. Chu, Microfluidic preparation of multicompartment microcapsules for isolated coencapsulation and controlled release of diverse components, Int. J. Nonlinear Sci. Numer. Simul. **13**, 325 (2012).
[135] S. S. Lee, A. Abbaspourrad, and S. H. Kim, Nonspherical double emulsions with multiple distinct cores enveloped by ultrathin shells, ACS Appl. Mater. Interfaces **6**, 1294 (2014).
[136] Q. Wu, C. Yang, G. Liu, W. Xu, Z. Zhu, T. Si, and R. X. Xu, Multiplex coaxial flow focusing for producing multicompartment Janus microcapsules with tunable material compositions and structural characteristics, Lab Chip **17**, 3168 (2017).
[137] Y. Hu, Q. Wang, J. Wang, J. Zhu, H. Wang, and Y. Yang, Shape controllable microgel particles prepared by microfluidic combining external ionic crosslinking, Biomicrofluidics **6**, 026502 (2012).
[138] Y. Hu, G. Azadi, and A. M. Ardekani, Microfluidic fabrication of shape-tunable alginate microgels: Effect of size and impact velocity, Carbohydr. Polym. **120**, 38 (2015).
[139] E. Mele, D. Fragouli, R. Ruffilli, G. L. De Gregorio, R. Cingolani, and A. Athanassiou, Complex architectures formed by alginate drops floating on liquid surfaces, Soft Matter **9**, 6338 (2013).
[140] See Supplemental Material at http://link.aps.org/supplemental/10.1103/PhysRevFluids.3.093601 for further details on laboratory procedures, parameters, theory, and comparison between experiments and computer simulations.
[141] Z. C. Feng and L. G. Leal, Numerical simulation of the dynamics of an electrostatically levitated drop, Int. J. Multiphase Flow **22**, 93 (1996).
[142] A. Ramachandran, K. Tsiglifis, and L. G. Leal, Properties and solution techniques for a mixed type boundary integral equation arising in creeping flow problems, Comput. Fluids **64**, 141 (2012).
[143] H. A. Stone and L. G. Leal, Relaxation and breakup of an initially extended drop in an otherwise quiescent fluid, J. Fluid Mech. **198**, 399 (1989).
[144] A. Z. Zinchenko, M. A. Rother, and R. H. Davis, A novel boundary-integral algorithm for viscous interaction of deformable drops, Phys. Fluids **9**, 1493 (1997).
[145] A. Z. Zinchenko, M. A. Rother, and R. H. Davis, Cusping, capture, and breakup of interacting drops by a curvatureless boundary-integral algorithm, J. Fluid Mech. **391**, 249 (1999).
[146] P. Murrell, *R Graphics, Second Edition* (CRC Press, Boca Raton, FL, 2012).